Available online at www.sciencedirect.com
ScienceDirect
C. R. Physique 8 (2007) 1184–1197
COMPTES RENDUS PHYSIQUE
http://france.elsevier.com/direct/COMREN/

Optical parametric sources for the infrared/Sources optiques paramétriques pour l'infrarouge

Parametric fluorescence in semiconductor waveguides

Marco Ravaro [a], Loïc Lanco [a], X. Marcadet [b], Sara Ducci [a], Vincent Berger [a], Giuseppe Leo [a,*]

[a] *Laboratoire matériaux et phénomènes quantiques, CNRS–UMR 7162, Université Paris–Diderot, bâtiment Condorcet, BP 7021, 75205 Paris cedex 13, France*

[b] *Alcatel–Thales III–V Lab, TR&T, route départementale 128, 91767 Palaiseau, France*

Available online 7 November 2007

Abstract

We report on semiconductor waveguides for room-temperature parametric fluorescence in the near infrared. Two phase-matching schemes are presented: form birefringence and counter-propagating phase matching. The characteristics and performances of these solutions are discussed and compared for different kinds of applications. The emergence of these devices opens new perspectives toward guided-wave parametric amplifiers, oscillators, and sources for quantum information. ***To cite this article: M. Ravaro et al., C. R. Physique 8 (2007).***

Résumé

Fluorescence paramétrique en guides d'ondes semiconducteurs. Nous présentons nos résultats sur des guides d'ondes semiconducteurs pour la fluorescence paramétrique dans le proche infrarouge. Deux schémas d'accord de phase sont présentés : la biréfringence de forme et l'accord de phase contrapropageant. Les caractéristiques et les performances de ces solutions sont analysées et comparées pour différents types d'applications. L'émergence de ces dispositifs ouvre des nouvelles perspectives vers la réalisation d'amplificateurs paramétriques, oscillateurs et sources pour l'information quantique en régime guidé. ***Pour citer cet article : M. Ravaro et al., C. R. Physique 8 (2007).***

Keywords: Semiconductor waveguides; Parametric fluorescence; Quantum information

Mots-clés : Guides d'ondes semiconducteurs ; Fluorescence paramétrique ; Information quantique

1. Introduction

New optical sources in the near- and mid-infrared have recently attracted a growing attention for potential applications in telecommunication systems [1], spectroscopy [2,3], gas sensing [4], and quantum information [5,6]. In this respect, parametric fluorescence (PF) is an interesting process due to its relative simplicity and to the tunability of the output wavelengths. PF is a three-wave-mixing process occurring in a non-centrosymmetric medium, with one input pump wave and two signal and idler output fields. Pump (p), signal (s) and idler (i) frequencies obey energy

* Corresponding author.
E-mail address: giuseppe.leo@univ-paris-diderot.fr (G. Leo).

1631-0705/$ – see front matter
doi:10.1016/j.crhy.2007.09.006

conservation ($\omega_p = \omega_s + \omega_i$). Moreover, in order to have a high efficiency, a phase-matching (PM) condition needs to be fulfilled, which corresponds to canceling the phase-velocity mismatch between the interacting waves [7].

Historically, the first $\chi^{(2)}$ materials used to fulfill the PM condition were birefringent crystals, the refractive index of which depends on the field polarization in the medium [8]. In uniaxial media, in particular, one of the two indices (called 'extraordinary') varies with the propagation angle of the beam with respect to the optical axis, which allows it to fulfill a birefringent PM condition through a proper crystal orientation.

In general, a high nonlinear optical performance is obtained for a high-intensity pump and phase-matchable materials with high nonlinearity.

As far as the sources are concerned, a high degree of both spatial and temporal coherence is required. Spatial coherence, allowing a small diffraction angle when a beam is focused in a crystal, results in high intensity and increased 'effective' interaction length (i.e. high parametric gain), plus low spatial dispersion (i.e. better phase-matching capability). Temporal coherence, implying a high monochromaticity, results in a better PM capability as well.

As far as the materials are concerned, non-centrosymmetry is the basic requirement and, in principle, highly-nonlinear crystals can be found on the guidelines of Miller's rule (i.e. looking for highly-refractive materials) [9]. For birefringent PM, several properties are required besides optical anisotropy: sufficient birefringence for phase-matched generation of a wide range of frequencies; wide PM bandwidths; small walkoff between the ordinary and the extraordinary ray; noncritical phase-matchability. For pulsed interactions, in addition, both small group-velocity mismatch and small group-velocity dispersion are key issues.

Further requirements that often play a decisive role in the materials' success are: wide transmission range at ω_p, ω_s, ω_i; high optical-damage threshold; low transmission losses; good thermal, chemical and mechanical properties; availability in bulk form and large size; and finally, from our point of view, the possibility to host an optical waveguide. The number and the relevance of the above considerations make it not surprising that no material has been found yet, which is capable to satisfy all the above requirements.

Broadly speaking, there are three main classes of nonlinear optical materials: inorganics, organics, and semiconductors. Since the early days of nonlinear optics, inorganics have been the most popular $\chi^{(2)}$ materials. Progress in material science during the last three decades allowed the widespread use of the moderately-nonlinear, birefringent ferroelectrics $LiNbO_3$, $KNbO_3$, KTP in the visible–near IR region. Finally, for frequency generation down to the UV, widely-angle-tunable, weakly-nonlinear borates like BBO are mostly employed, whereas chalcopyrites are used in mid IR (beyond 10 μm) [10]. Organic materials, essentially amounting to Langmuir–Blodgett films [11], poled polymers like DANS [12], and salt crystals like DAST [13], exhibit high to gigantic nonlinearities, albeit at the price of a narrow transparency spectral window and high waveguide losses. Semiconductors like GaAs, which are readily available from electronic technology, are highly nonlinear and exhibit below-gap transparency. However, their cubic point-group symmetry makes them optically isotropic, which hampers birefringent PM.

Summarizing: not all of the above materials are apt to host waveguides; in the material of choice, a tradeoff occurs between nonlinearity and transparency bandwidth; and the prevailing PM approach to date is still birefringent PM, with the related wavelengths and temperatures set by natural coincidences in material parameters. A microelectronics-like scenario, where mastering growth and processing of a limited number of materials allows one to tailor a large number of functional devices, is still lacking. For practical reasons, it is highly desirable that material engineering and microstructuring could eventually relax the natural constraints of nonlinear optical materials. This has begun to be the case for the quasi-phase matching (QPM) approach [14], which has proven successful not only in ferroelectrics like periodically-poled $LiNbO_3$ (PPLN) [15] and KTP (PPKTP) [16], but also in periodically-reversed GaAs [17].

Restricting our scope to nonlinear optical waveguides, the most mature PPLN technology has already resulted in high-performance integrated OPOs [18], whereas the first demonstrations of second harmonic generation (SHG) in PPKTP and QPM AlGaAs waveguides have been reported recently [19,20].

The motivation of our activity on GaAs nonlinear waveguides stems from our belief that periodically-poled ferroelectric waveguides are not the best candidates for playing the role of 'silicon' in the integrated nonlinear optics of the future. We think that in the long term, because of the perspective of a full optoelectronic integration with circuitry, diode lasers and photodiodes, direct-bandgap III–V semiconductors will prevail.

In the last years, GaAs nonlinear waveguides have attracted a great deal of attention because of their huge nonlinearities [21], room temperature operation, and well-mastered growth and processing techniques. In the framework of nonlinear-optics-oriented semiconductor engineering, several PM approaches have been proposed. While deferring to the paper of M.M. Fejer [22], where low losses still constitute a challenging task to date, let us focus here on

two alternative routes for perfect PM in semiconductor waveguides: form-birefringence PM (Section 2) and counter-propagating PM (Section 3). Finally, in Section 4, we discuss and compare the characteristics of these two approaches for different kinds of applications.

2. Form birefringence phase matching

2.1. Design and fabrication

Form-birefringence PM is obtained by using the artificial birefringence of a composite multilayer material: the isotropy of bulk GaAs is broken by inserting thin oxidized AlAs (AlOx) layers. The idea has been proposed in a pioneering paper of Van de Ziel in 1975, [23], but the experimental realization of form-birefringence PM has been achieved only in 1997, when the development of oxidation techniques [24] has permitted the realization of a well suited pair of materials having a high nonlinear coefficient and a sufficient refractive index contrast [25].

The principle of form birefringence can be understood by making some symmetry considerations on the crystalline structure of this artificial material. The presence of thin AlOx layers on a (100) GaAs substrate breaks the symmetry of 3-fold rotation axes of the GaAs and the point group of the composite material becomes $\bar{4}2m$, i.e. the same as KDP. In this way we obtain a material with the same nonlinear properties as GaAs (the small zero contribution of the thin AlOx layers can be neglected), and the linear optical properties of KDP. For a periodic layered medium and a propagation direction, it can be shown that:

$$n_{\mathrm{TE}}^2 = \frac{h_1}{\Lambda} n_1^2 + \frac{h_2}{\Lambda} n_2^2$$

$$\frac{1}{n_{\mathrm{TM}}^2} = \frac{h_1}{\Lambda}\frac{1}{n_1^2} + \frac{h_2}{\Lambda}\frac{1}{n_2^2}$$

with Λ the period and $h_i\,(n_i)$ the thickness (refractive index) of the ith repeated layer ($i = 1, 2$; $h_1 + h_2 = \Lambda \ll \lambda$).

Form birefringence ($n_{\mathrm{TE}} - n_{\mathrm{TM}}$) occurs due to different boundary conditions for E_{TE} and E_{TM}: in the TM polarization, the continuity of the electric displacement forces the electric field to have a large value in the low-index material. This is illustrated on Fig. 1, which presents a typical heterostructure, grown by molecular beam epitaxy (MBE) on GaAs (001) substrates with the structure: 1000 nm $Al_{0.92}Ga_{0.08}As$/1000 nm $Al_{0.7}Ga_{0.3}As$/4× (37 nm AlAs/273 nm GaAs)/37 nm AlAs/1000 nm $Al_{0.7}Ga_{0.3}As$/30 nm. After the growth AlAs layers are converted in amorphous AlOx layers ($n \approx 1.6$) by lateral selective oxidation. This structure is designed such that, after the oxidation process, it is phase matched for a degenerate three wave mixing process between a TM_0 photon at 1.06 μm and two TE_0 photons at 2.12 μm [26].

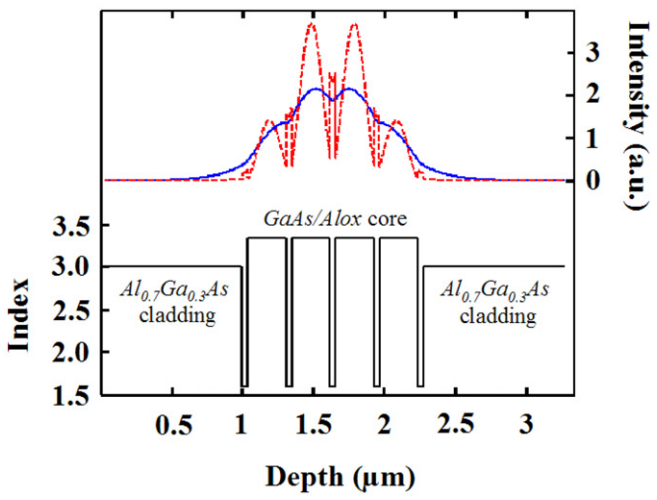

Fig. 1. Refractive index profile (2.128 μm) and intensity distribution of the modes TE_0 (solid line) at 2.128 μm and TM_0 (dashed line) at 1.064 μm. The epitaxial structure of the waveguide is described in the text.

2.2. Experimental results and perspectives

The first achievement of form-birefringent PM in an AlOx-based heterostructure was demonstrated with a mid-infrared difference frequency generation (DFG) from two near-infrared guided waves [27]. Two continuous-wave (CW) pump lasers were end-fire coupled in a GaAs/AlOx waveguide: a TE polarized Nd:YAG laser at 1.32 μm and a tunable, TM polarized Ti:Sa laser. By tuning the Ti:Sa wavelength a DFG process occurred, with maximum efficiency for the process: (1.035 μm, TM_0) − (1.32 μm, TE_0) → (4.8 μm, TE_0).

PF was first obtained a few years later in the same kind of structure [28]. In this case a CW Ti:Sa laser, tunable from 950 to 1070 nm, was coupled into a 3.2 mm-long waveguide and the PF signal was detected with an InSb detector, the pump being completely absorbed by a germanium filter. As expected from the selection rules imposed by the crystal symmetry and by the PM condition, signal and idler are TE polarized for a TM polarized pump. Moreover, due to the spectral broadening at degeneracy typical of type I process, the spectrally integrated PF output increases rapidly as the degeneracy is approached, whereas at a longer pump wavelength almost no photons are generated because phase matched down-conversion is forbidden.

The main limitation of these results consisted in waveguide optical losses, which could not be reduced to less than 4 dB cm^{-1}. These originate from optical defects at the AlOx layers interfaces, as shown from spectroscopic and TEM analyses [29,30].

Today our AlGaAs/AlOx nonlinear waveguides are of the type shown in the scanning-electron-microscope (SEM) picture of Fig. 2. Lateral confinement is provided by ≈3 μm-wide ridges, which are wet etched along GaAs ⟨110⟩ direction in order to optimally exploit the nonzero component of the nonlinear susceptibility tensor. A parametric gain coefficient $g = 4.83\ cm^{-1}\,W^{-1/2}$ is calculated in a lossless case, where the effective area is approximated with 1D vertical mode profiles multiplied by an effective mode width, following the effective-index method.

In these samples, thanks to processing optimization, we reproducibly achieve record losses as low as 2 dB cm^{-1} at 1.55 μm, which we measured with a multimode Fabry–Perot method [31]. We ascribe these residual losses to guided-mode scattering at the interfaces between oxidized and crystalline layers [30]. Conversely, virtually no losses are caused by the ridge side-wall roughness, which we estimate to less than 2 nm rms, with atomic-force microscopy.

In these multilayer GaAs/AlOx waveguides we have recently performed new PF experiments, with significant improvements. By end-fire coupling a TM polarized Ti:Sa CW pump beam into the waveguide, we have measured the

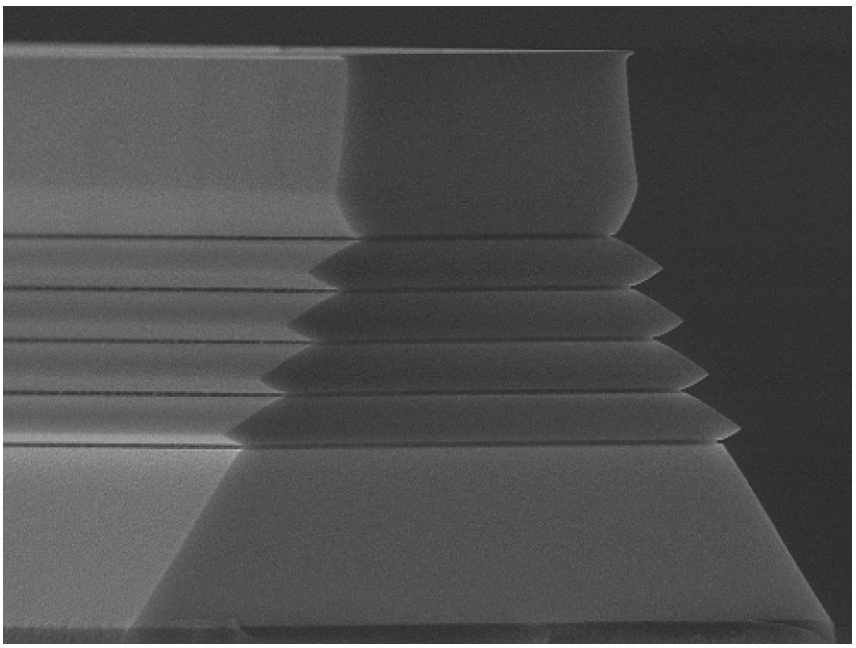

Fig. 2. Scanning-electron-microscope picture of the partially oxidized AlGaAs multilayer waveguide. The non-conventional transverse profile is longitudinally invariant and therefore affects by no means the optical losses.

tuning curve (i.e. the wavelengths of the down-converted beams versus the pump wavelength) reported in Fig. 3. In this sample we have found the first evidence of parametric gain, and we have confirmed the inferred value of parametric gain coefficient by measuring SHG conversion efficiency with a CW low power input of 2.1 μm.

As shown in Fig. 4, about 100 nW of signal power were achieved at degeneracy, with an internal conversion efficiency $\eta = (1.5 \pm 0.3) \times 10^{-6}$. Moreover, as expected at this pumping level, the signal output power seems to exhibit a slight nonlinear dependence on in-coupled pump power P_p, which is a signature of parametric amplification. In Fig. 5 we compare two experimental emission spectra, at degeneracy and at 0.2 nm off degeneracy: in agreement with design predictions, wide tunability can be accomplished by slightly changing pump wavelength or sample temperature. By

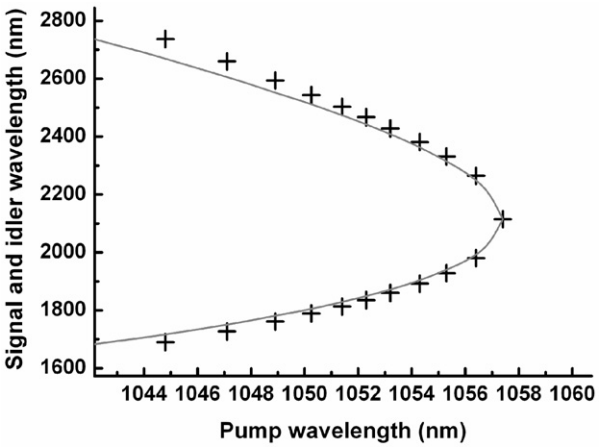

Fig. 3. Signal and idler wavelengths vs. Ti:Sa pump wavelength. Solid line: calculated parametric tuning curve; crosses: experimental data. Experimental twin points correspond to a single measurement: one wavelength has been measured, and the other one has been reported considering energy conservation.

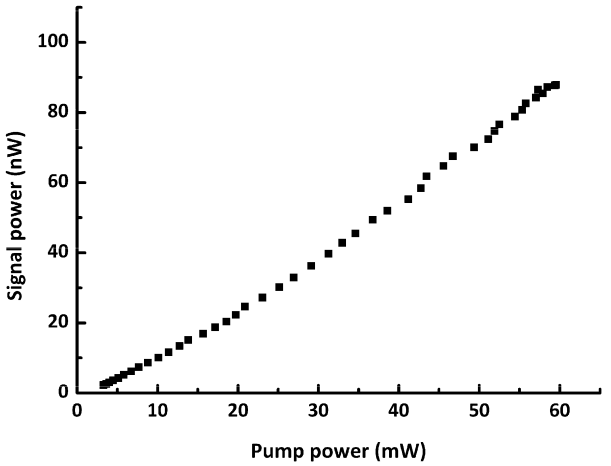

Fig. 4. PF signal power at degeneracy vs. CW pump power.

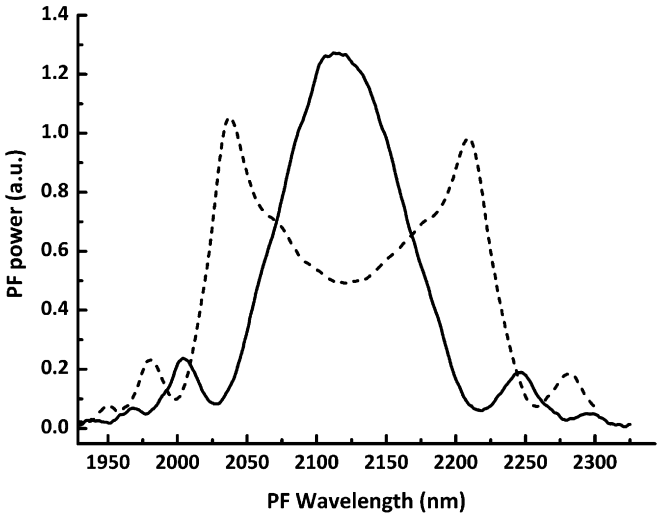

Fig. 5. PF spectra at degeneracy (solid line) and 0.2 nm off degeneracy (dotted line).

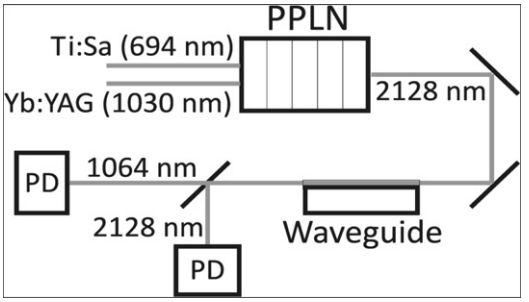

Fig. 6. SHG experiment setup, with a CW pump source at 2.128 μm obtained through DFG between a Ti:Sa ($\lambda = 694$ nm, FWHM = 1.5 GHz) and a Yb:YAG ($\lambda = 1030$ nm, FWHM = 5 MHz) beams in a PPLN crystal (4 cm-length, AR coatings, MgO doping, 15 μm QPM period, $T = 170°C$).

calculating the idler input as the vacuum fluctuations integrated on the phase-matching band [32], we may infer the parametric gain coefficient $g = (4.0 \pm 0.7)\sqrt{P_p}\ \mathrm{cm}^{-1}$ from the experimental efficiency. To validate this value independently on the actual phase-matching spectrum, especially in a strongly temperature-sensitive device at high CW pumping intensities ($>1\ \mathrm{MW\,cm}^{-2}$), this crucial parameter was further evaluated by measuring frequency doubling conversion efficiency in the same waveguide.

We performed this SHG experiment with a narrow-linewidth, TE polarized, low power, CW pump source at 2.128 μm. The latter was obtained through DFG in a PPLN crystal, with the setup detailed in Fig. 6. As the pump wavelength was not continuously tunable, we performed the SHG experiment by using the waveguide temperature as a control parameter (the latter was varied with a Peltier module). The PM curve is shown in Fig. 7, where the deviation from the ideal sinc^2 shape can be ascribed to temperature inhomogeneity along the sample and to a slight drift of the ridge width along propagation. Note that the latter can be estimated to less than 100 nm after scanning-electron-microscope observation, resulting in a PM wavelength shift smaller than the calculated full width at half maximum (FWHM). Second-harmonic versus fundamental-frequency power at PM is reported in Fig. 8, after careful setup calibration: $134\%\ \mathrm{W}^{-1}$ internal conversion efficiency was inferred by a quadratic fit of the experimental data. This corresponds to a normalized conversion efficiency of $1500\%\ \mathrm{W}^{-1}\,\mathrm{cm}^{-2}$, which is the highest ever reported for frequency doubling in low-loss AlGaAs waveguides. In terms of parametric gain, this corresponds to $g = 3.9 \pm 0.7\ \mathrm{cm}^{-1}\,\mathrm{W}^{-1/2}$, i.e. slightly less than the calculated value, and in good agreement with the value inferred by the parametric fluorescence experiment.

We want to stress that the above PF exhibits unprecedented signal-to-noise ratios in form-birefringent, longitudinally uniform GaAs waveguides. These results open the way to the fabrication of monolithic parametric amplifiers and oscillators around 2 μm [33]. As the semiconductor laser sources that could be used to pump this device are usually poorly tunable, the large opening of the tuning curve results in a great advantage: small variations of the pump wavelength are sufficient to provide a very wide tunability of the output wavelengths, between 1.4 and 3.5 microns.

The availability of a compact mid-infrared OPO would be of a great impact to environmental problems (in particular gas sensing). With comparison to traditional chemical probes, absorption spectroscopy offers the advantage of weak maintenance costs, rapid responses, and remote sensing.

By taking into account the measured efficiency of parametric emission and the value of optical losses [34], a doubly resonant system provided with 90% dielectric mirrors should have a pump threshold of 100 mW. A technological study is in progress to acquire a deeper comprehension of the oxidation process and to improve the reflectivity of the mirror deposited onto the waveguide facet. This will, hopefully, allow the reduction of optical losses and consequently the value of oscillation threshold.

So far, the heterostructures described in this section do not make use of one of the principal advantages of III–V semiconductors with respect to other nonlinear materials: the integrability of an internal quantum-well laser pump in the core of the waveguide. The possible electrical pumping of an on-chip GaAs/AlOx nonlinear device is made

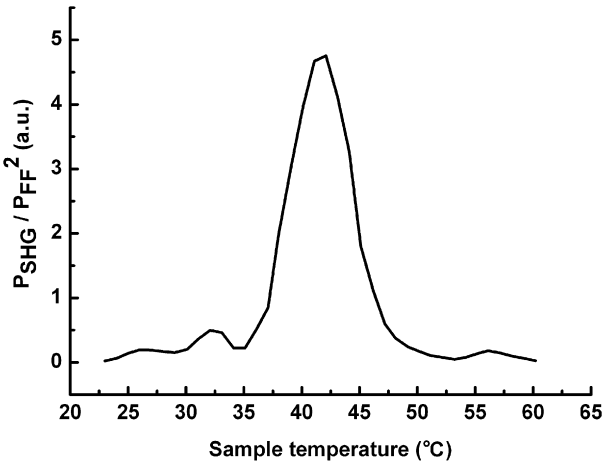

Fig. 7. SHG PM curve vs. temperature measured in a 3 mm-long waveguide, with a fundamental-frequency wavelength of 2.128 μm.

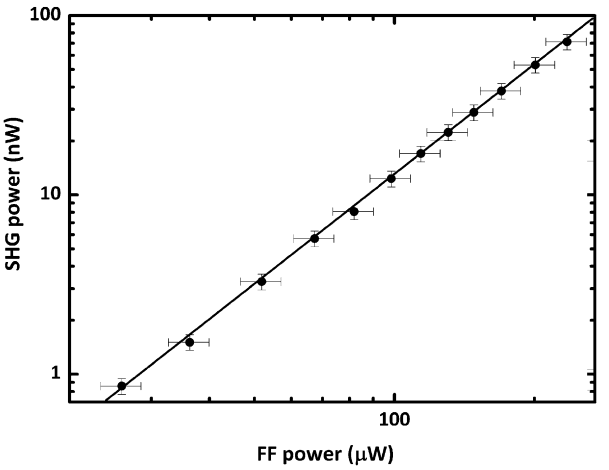

Fig. 8. Phase-matched SHG versus fundamental-frequency power in the form-birefringent waveguide.

arduous by the insulating nature of the oxidized layers, and electrical transport is not fully compatible with the present form-birefringent structure. A higher degree of compactness is possible with an oxide-free parametric source, which is described in the next section.

3. Counter-propagating phase matching

3.1. Design and fabrication

In the scheme sketched in Fig. 9 a transverse pump beam propagating across the heterostructure interacts with two counter-propagating orthogonally-polarized modes of an AlGaAs waveguide [33,35,36]. This geometry allows PM in the longitudinal (z) direction; for each angle of incidence θ of the pump beam, the z component of the pump wavevector k_p compensates the mismatch, $k_s - k_i$, between the signal and idler k vectors: $\Delta k = k_p \sin\theta + k_i - k_s = 0$. In the epitaxial ($x$) direction quasi-phase-matching is implemented—through an alternation of $\lambda_p/2$ layers with nonlinear coefficients d_{14} as different as possible—in order to maximize the efficiency of the nonlinear process [37].

The most attractive application of a such heterostructure is the parametric generation of counter-propagating twin photons in the fiber telecom bandwidth. Important advantages of this scheme, in the aim of realizing quantum communication devices, result from this geometry: room-temperature operation, absence of the pump beam in the guided direction, easy separation and coupling of the down-converted photons into optical fibers, easy tunability through the incident angle of the pump beam, and narrow spectral bandwidth (near the Fourier transform limit) due to counter-propagation [38].

The $\chi^{(2)}$ tensor of AlGaAs allows type-II interactions, where one of the down-converted photon is TE polarized, and the other one is TM polarized. This results in two ways to cancel the phase mismatch in the z direction: either the signal is TE polarized and the idler is TM polarized (which we shall refer to as interaction "−"), or the signal is TM polarized and the idler is TE polarized (interaction "+").

The central frequencies for the signal and the idler are determined through the conservation of energy and of momentum in the z direction, leading to the following equations:

$$\begin{cases} l\omega_p = \omega_s + \omega_i \\ \omega_p \sin\theta = \omega_s n_{\mathrm{TE}}(\omega_s) - \omega_i n_{\mathrm{TM}}(\omega_i) \end{cases} \quad (-)$$

$$\begin{cases} \omega_p = \omega_s + \omega_i \\ \omega_p \sin\theta = \omega_s n_{\mathrm{TM}}(\omega_s) - \omega_i n_{\mathrm{TE}}(\omega_i) \end{cases} \quad (+)$$

Clearly, these frequencies depend on the incidence angle θ of the pump beam, which provides a very convenient mean to tune them.

Fig. 10 reports the dependency of the signal and idler wavelengths on θ, for a structure having the following epitaxial structure: 1081 nm $Al_{0.94}Ga_{0.06}As$ (cladding)/110 nm $Al_{0.25}Ga_{0.75}As$/4× [128 nm AlAs/110 nm $Al_{0.25}Ga_{0.75}As$]

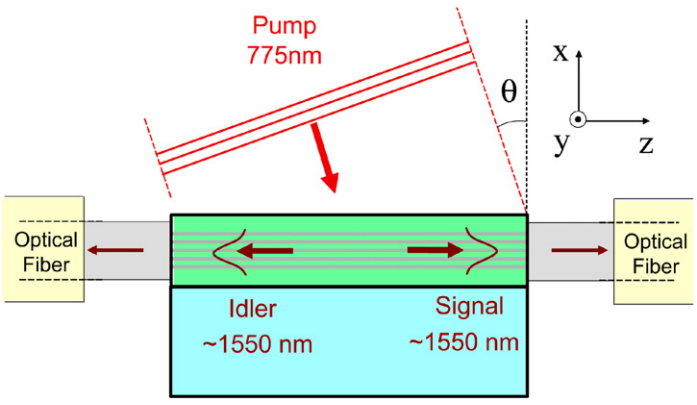

Fig. 9. Schematics of the counter-propagating parametric source. The z axis is along waveguide propagation and coincides with the ⟨110⟩ direction of GaAs. Pump incidence is at an angle θ with respect to the x axis (vertical confinement), and lateral confinement is along y.

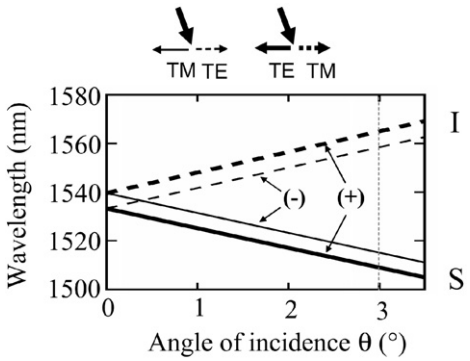

Fig. 10. Calculated tuning curves for a pump wavelength of 768.2 nm. Thick lines: additive interaction (+). Thin lines: subtractive interaction (−).

(core)/1081 nm $Al_{0.94}Ga_{0.06}As$ (upper cladding). In the X-shaped tuning curves typical of type-II interactions, note that the difference between the degeneration angles relative to interactions "−" and "+" is due to modal birefringence in the waveguide.

The sharing of the pump photon energy between signal and idler results in two concomitant effects: (1) a higher energy for the TM photon, because it travels faster than the TE photon due to birefringence; (2) a higher energy for the photon co-propagating with the z-projection of the pump beam, since it carries a supplementary momentum given by the pump. Additive contributions from these effects are thus obtained if the co-propagating photon is TM polarized and the counter-propagating one TE polarized: this is the case we have referred to as 'additive' (+) interaction. Conversely, the process with a TE co-propagating photon and a TM counter-propagating photon has been referred to as 'subtractive' (−) interaction. In the calculated tuning curves of Fig. 10, the additive interaction is responsible for the longest and shortest emitted wavelengths, whereas the subtractive interaction is responsible for the intermediate ones. We point out that the two effects discussed above (birefringence and pumping geometry) can cancel out exactly, giving rise to wavelength-degenerate twin photons. As can be seen in Fig. 10, this occurs for $\theta = 0.4°$ in the subtractive interaction.

The spectrum of the down-converted photons has the usual $\mathrm{sinc}^2(\Delta k L/2)$ shape, where L is the waveguide length. One of the main advantages of counter-propagating geometry arises from the rapid increase of Δk when one moves off from perfect PM, which leads to a very narrow bandwidth for the down-converted photons. This is a favorable issue for this device, as chromatic dispersion can cause problems for some application. For example, quantum cryptography schemes implementing phase or phase-and-time coding rely on photons arriving at well-defined times, i.e. well localized in space. In dispersive media, like optical fibers, different group velocities are a source of noise for the localization of photons; for this reason the broadening of photon bandwidth must be circumvented or controlled [5]. In our device the spectral width of signal and idler is given by

$$\Delta\omega = \frac{5.57}{L}\left|\frac{1}{v_{gS}} + \frac{1}{v_{gI}}\right|^{-1}$$

where v_{gS} and v_{gI} are the signal and idler group velocities at perfect PM. For the above AlGaAs structure, with $L = 1$ mm and a perfectly collimated monochromatic pump, this corresponds to a wavelength bandwidth of 0.15 nm. We notice that, in co-propagating geometry, the sum of the group velocities is replaced by their difference in the previous expression, thus increasing the spectral width.

Furthermore, an interesting advantage of this scheme is that the combination of type-II phase-matching with counter-propagation for the signal and the idler leads naturally to polarization entanglement, as in the source of polarization-entangled photon pairs by Kwiat et al. [38]. The photon pair is generated in a superposition of the states produced by interactions "−" and "+". The weight of each of those states in the total state vector is related to the efficiency of the corresponding interaction. Namely, after removal of the vacuum component, it can be written as $(|\eta_-|^2 + |\eta_+|^2)^{-1/2}(\eta_-|\omega_{s,-}, \mathrm{TE}\rangle|\omega_{i,-}, \mathrm{TM}\rangle + \eta_+|\omega_{s,+}, \mathrm{TM}\rangle|\omega_{i,+}, \mathrm{TE}\rangle)$, where $|\eta_i|^2$ may be regarded as the efficiency of interaction i expressed in photon pairs per pump photon [39].

3.2. Experimental results and perspectives

From an experimental point of view, the difficulty is twofold: given the narrow angular acceptance for the pump beam, it is not trivial to find the PM condition; given the extremely low and uncertain predicted efficiency, the adequate detection scheme is not a priori evident. For these two reasons, two preliminary measurements were carried out on the same sample before the PF experiment, following the schemes of Fig. 11: a surface-emitted sum frequency generation experiment (SESFG) and a backward DFG experiment (BDFG) [40].

SESFG (Fig. 11(a)) is the reverse of the PF process of Fig. 9: two counter-propagating guided modes of wavelengths λ_i and λ_s, with respective polarizations TE and TM, generate a sum frequency field that radiates away from the waveguide at wavelength λ_p. The emission angle θ of this field is such that the longitudinal component of its wavevector compensates the phase velocity mismatch between the guided modes. In fact, θ can be precisely evaluated if both TE and TM modes are end-fire excited through the same input facet, relying on their Fresnel reflection at the opposite facet. By doing so, two nonlinear processes occur: the interaction of the TE mode with the reflected part of the TM one, and the interaction of the TM mode with the reflected part of the TE one. This symmetric configuration results in the generation of two sum-frequency waves of comparable amplitudes, which radiate with angles θ and -θ, respectively: an interference pattern can thus be observed at the waveguide surface, whose period Λ provides a straightforward measure of θ through the relation $|\sin\theta| = \lambda_p/2\Lambda$. In detail, two cw laser beams tunable in the telecom range, respectively TE- and TM-polarized, are end-fire-coupled into the input facet of the waveguide. Some of the near-field SESFG interference patterns, as acquired with a microscope and a CCD camera mounted over the waveguide, are shown in Fig. 12(a) for different sets of injected wavelengths, with $(1/\lambda_s + 1/\lambda_i)^{-1} = \lambda^p = 780$ nm. The first pattern corresponds to the degenerate case $\lambda_s = \lambda_i$, where the phase velocity mismatch is due to the slight modal birefringence of the heterostructure. In the second pattern, exhibiting the longest period i.e. the smallest phase velocity mismatch, the birefringence effect is compensated for by a suitable wavelength difference $\lambda_s - \lambda_i$. In the third to fifth pattern, the period gets shorter and shorter as the phase velocity mismatch increases with the difference $\lambda_s - \lambda_i$. The related tuning curve is plotted in Fig. 12(b), where an excellent agreement can be appreciated between experimental data and numerical predictions. The results of Fig. 12(b) provide us with solid grounds on the experimental relation between λ_s, λ_i and θ at phase matching.

In the BDFG experiment (Fig. 11(b)) the out-of plane pump beam was provided by a CW Ti:Sa laser and was engineered to illuminate the waveguide in the most efficient way: (1) in the xz plane, the beam is carefully collimated, such that a virtually flat wavefront impinges on the waveguide with a determinate value of θ; (2) in the y direction, the beam is focused with a cylindrical lens, in order to provide an optimum overlap with the waveguide ridge. For the pump we have set a power $P_p = 70 \pm 10$ mW, an angle $\theta = 4.3 \pm 0.1°$, and a wavelength $\lambda_p = 780$ nm. From Fig. 12(b) we know that a TE mode with $\lambda_i \approx 1.60$ μm is phase-matched with a TM-polarized DFG signal with $\lambda_s \approx 1.52$ μm. The TE mode is excited by an external-cavity CW tunable laser beam, amplified with an Er^+-doped fiber, spectrally filtered with a monochromator, and end-fire-coupled into the waveguide. Here again, we have preferred to rely on Fresnel reflection: the BDFG signal is generated from the reflected part of the TE mode at the opposite facet, such that both the throughput at λ_i and signal at λ_s are collected at this facet. Once collimated, they are separated by a

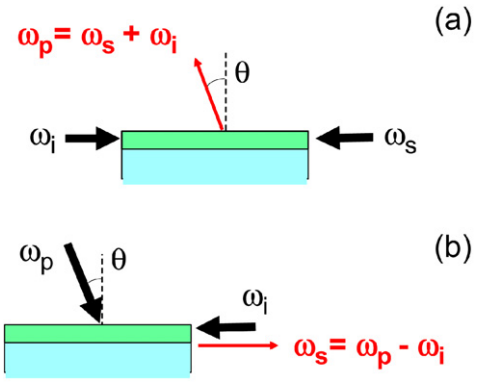

Fig. 11. Conceptual schemes of SESFG (a) and BDFG (b) experiments.

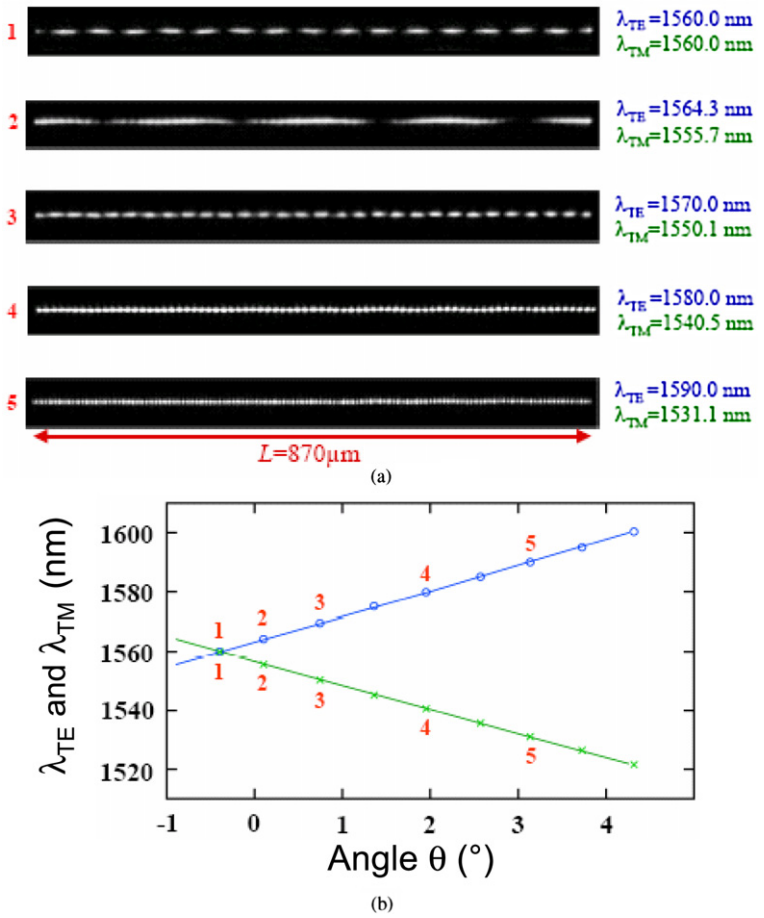

Fig. 12. (a) SESFG patterns at $\lambda_p = 780$ nm, for different pairs of λ_i (TE) and λ_s (TM). (b) Tuning curve of the device, as a function of the emission angle θ. Open circles (λ_i) and crosses (λ_s) represent the experimental points (numbers correspond to the patterns shown in (a) and solid lines result from numerical simulations.

polarizing beamsplitter: the former is reflected towards a large-area Ge photodiode, while the latter is transmitted towards a low-noise InGaAs photodiode through the band-pass interference filters. The InGaAs photodiode feeds a high-gain amplifier followed by a lock-in amplifier, with a noise equivalent power of 1 pW. As expected, BDFG is observed for λ_i between 1601.4 and 1602.2 nm. At the phase matching wavelength $\lambda_{PM} = 1601.8$ nm, we obtained an intrinsic conversion efficiency $\eta = P_s/P_i P_p = (3.5 \pm 2) \times 10^{-6}\ \mathrm{W}^{-1}$. The BDFG spectrum is shown in Fig. 13, where the observed sinc^2 curve is a clear signature of a phase matched process; at PM, the wavelength generated is $\lambda_s = 1520.3$ nm. Besides knowing the PM bandwidth of this counter-propagating interaction, from the BDFG experiment we learn one basic fact: for the PF experiment the above photodiode detection scheme is not sufficient and we need two single-photon detectors.

Finally, the setup for the PF experiment is shown in Fig. 14: the pump beam is provided by a TE polarized, pulsed Ti:Sa laser with $\lambda_P = 768.2$ nm and a 3 kHz repetition rate. The pulse peak power is $P_p = 100$ W and its duration is 100 ns. The pump beam is focused on top of the waveguide ridge using a cylindrical lens with an angle θ in the xz plane. The generated photons are collected with two microscope objectives, spectrally analyzed with two monochromators, and then coupled into fibered InGaAs single-photon avalanche photodiodes. With this setup we measured the spectral profiles of the generated photons, which are given by the count rate recorded by each detector versus wavelength. These are shown in Fig. 15 for $\theta = 3°$, where sharp peaks are superposed on a flat background. The spectral structure nicely corresponds to the expected counter-propagating processes of Fig. 10 (dashed line at $\theta = 3°$): the longest and shortest wavelengths result from the additive process, while the intermediate ones result from the subtractive interaction. A complete agreement is found between experimental values and numerical simulations of the

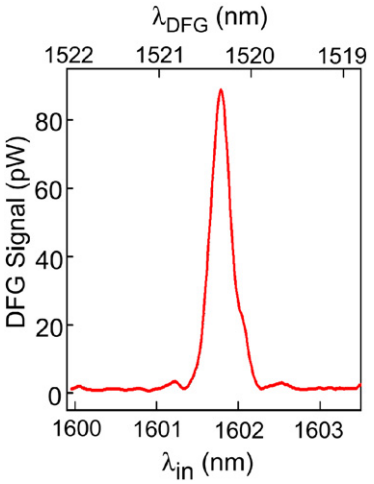

Fig. 13. Experimental BDFG signal, corresponding to $P_i = 350$ μW and $P_p = 70$ mW. The generated wavelength is deduced from the input wavelength through $\lambda_s = (1/\lambda_p - 1/\lambda_i)^{-1}$.

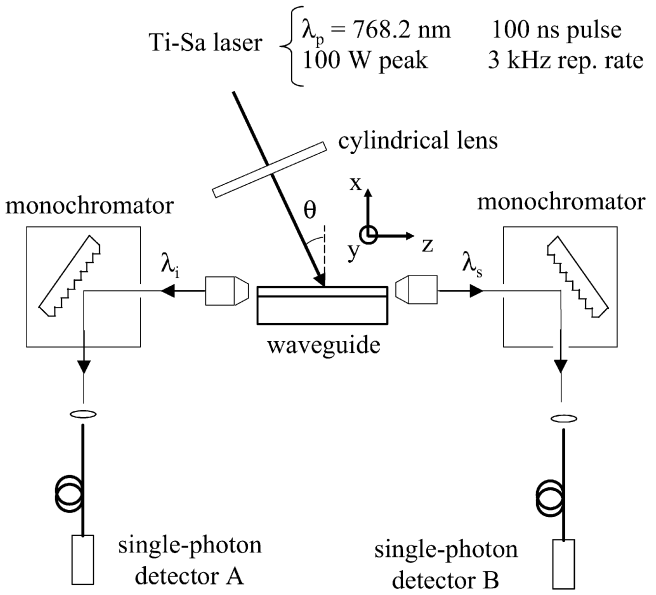

Fig. 14. Experimental setup for the PF in the counter-propagating geometry.

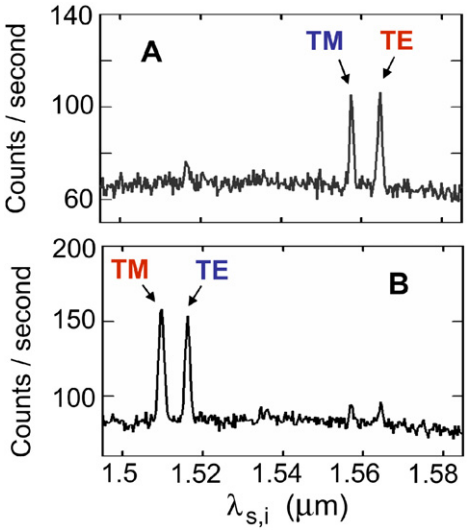

Fig. 15. Emission spectra for an angle of incidence of 3°. The spectra A and B are acquired by the detectors A and B of Fig. 14, respectively. Signal photons, which co-propagate with the z component of the pump and impinge on the detector b, carry a supplementary momentum and thus have a lower wavelength. In both spectra TM photons have a lower wavelength than the TE ones, corresponding to their higher propagation velocity in the multilayer waveguide. The small secondary peaks result from generated photons that undergo a reflection at a waveguide facet before impinging on the detector A or B.

generated wavelengths. Such a good agreement reflects the robustness of the structure with respect to the tolerances on the ridge size (width and height), and to the fluctuations (thickness and composition of the layers) in the MBE process.

The flat background in the measured spectra arises from two contributions: (1) dark counts generated by the detectors in the absence of any incident photon; and (2) photoluminescence due to electron–hole recombination after

pump absorption, resulting from below-bandgap deep levels embedded in semi-insulating GaAs substrates. In the future, both these contributions could be reduced: the former by employing state-of-the-art detectors and the latter by partially removing the substrate.

Moreover, significant improvements in quantum efficiency and background noise suppression are expected with a structure including Bragg mirrors to enhance the light-matter interaction and by removing the GaAs substrate, source of spurious deep level emission events. These modifications (especially the microcavity immersion) will lower the pump power to standard pump sources below the Watt level.

Finally, we emphasize the possibility of directly generating polarization-entangled states. For example, the generation of a Bell state can be done by simultaneously pumping the sample with $\theta = \pm 0.4^\circ$ (see Fig. 10), by illuminating the waveguide through a diffraction grating, or by inserting it in a bow-tie cavity.

Clearly, our twin photon source can be profitably integrated in innovative devices. On the one hand, one can e.g. obtain an entangled light emitting diode thanks to the integration of an electrically-pumped vertical cavity surface-emitting laser on top of the waveguide. On the other hand, forgetting entanglement but making use of simultaneity, an integrated heralded source of single photons is readily available by integrating or pigtailing a photon counter at one of the two waveguide facets.

4. Comparative analysis

Many analogies and differences occur between the two devices described above. Hereafter we want to discuss and compare their characteristics and performances. A summary of this discussion is given in Table 1.

Although both devices are passive, they exhibit markedly different perspectives in terms of pump-source laser integration. In the case of form birefringence, the need for a pair of materials with a sufficient index contrast leads to the oxidation of the AlAs layers; therefore, due to the insulating nature of the oxide, an electrical transport within the structure is not trivial. We can consider the option of optically pumping a possible laser-diode source at ω_p, but a detailed investigation is necessary to ensure that the proximity of the AlOx is not a problem for the radiative efficiency of the emitters. Also the present version of counter-propagating signal and idler geometry involves an external laser pump. In this case, however, a development can be envisaged with the integration of a VCSEL on top of the waveguide. In this case, the emitted photons will have a fixed wavelength as the angle of incidence would be fixed.

The frequency conversion range of the two devices described is linked to the transparency window for the materials used, the availability of pump source wavelength and the phase matching condition. The transparency range for AlGaAs is very broad: the limits are given by the phononic resonance (∼30 μm) and by the band-gap energy. The direct band-gap energy at room temperature goes from 1.42 eV (∼870 nm) for GaAs to 2.8 eV (∼443 nm) for AlAs [41].

Concerning the parametric efficiency, a few remarks are in order: in the case of co-propagating signal and idler (form birefringence) the efficiency depends quadratically on the sample length L, which explains why the efficiency is normalized to L^2 in the Table 1. In the case of counter-propagating signal and idler, on the contrary, the efficiency does not depend on L (of course, in this reasoning optical losses are not taken into account).

Another discriminating issue is the bandwidth of the generated signal; the counter-propagating geometry allows us to generate a spectrally narrow signal, which can constitute an advantage compared with what is obtained in the co-propagating geometry. We notice that the greater refractive index dispersion of GaAs with respect to usual nonlinear crystals makes our PM resonances narrower, for equal geometries.

Table 1
Synopsis of the characteristics and performance of the devices presented in this article

	Form-birefringence PM	Counter-propagating PM
Twin photons wavelength (realized)	2.1 μm (E)	1.55 μm (E)
Twin photons wavelength (possible)	1.55 μm	0.8–1.55 μm
Signal spectral width at degeneracy	∼150 nm (E)	∼0.15 nm (E)
PF efficiency	1.5×10^{-6} W/W (E)	2.5×10^{-14} W/W (E)
Optical losses (TE polarization)	1 cm^{-1} at 2.1 μm (E)	0.25 cm^{-1} at 1.55 μm (E)
Sensitive parameter for PM wavelength	Thickness of GaAs layer Refractive index of AlOx (T)	Very stable and easily tunable (T)

Optical waveguide losses are another crucial feature of our devices: the method we generally use to measure them is based on Fabry–Perot transmission fringes, and is well established for single-mode optical waveguides. We have recently proposed an extension of this technique to the case of multimode and tightly confining semiconductor waveguides [31]. This procedure involves Fabry–Perot measurements on a large spectral range, in order to find an interval where multimode effects do not alter the loss measurements. The validity domain of this method does not include form-birefringent samples; the loss measurement reported in Table 1 was obtained with a scattering technique using femtosecond pulses [34].

For the two kinds of devices, optical ridges are defined by chemical etching; the heterostructures based on modal phase matching and counter-propagating geometries are affected by relatively low losses. In form-birefringent samples, optical losses (0.5 cm^{-1}) have two main origins: scattering (especially at the interface with the oxide) and two-photon absorption. A morphologic investigation is in progress, in order to study the oxide interface under different growth and oxidation conditions; this will hopefully lead to a deeper insight of AlOx and to a reduction of optical losses.

An additional important point for our devices is the systematic analysis of how parameter variations in the structure (layer thicknesses, alloy composition, refractive indexes) affect the parametric tuning curves. This analysis is important for any practical design, in order to asses the tolerances in growth step and knowledge of the refractive indexes [26]. For each of the two devices, we have looked for the most sensitive parameter for frequency conversion.

In the case of form-birefringent structures the thickness of GaAs layers has to be controlled most homogeneously: a 1% relative variation of the thickness induces a 6 nm shift of the pump wavelength at degeneracy [25]. Another crucial point for these structures is the precise knowledge of the AlOx refractive index, which depends on the oxidation conditions (mainly oxidation time and temperature, thickness of AlAs layers). A variation of 0.03 of this index can induce a shift of 10 nm from the degenerate pump wavelength.

Concerning the counter-propagating geometry our calculations show that the structure is very stable with respect to the variation of both thickness and composition of the layers; the most sensitive parameter is aluminum concentration: as an example, a relative variation of 5% induces a variation in the signal wavelength of 0.1%, for an angle of incidence of 20°.

Note that the results given here are obtained by performing most numerical analysis in the planar waveguide approximation, and validating these with a few two- and three-dimensional simulations: 1D calculations prove quite satisfactory as far as the ridge is wider than 5 μm.

In conclusion, in this article we have illustrated our recent advances in the realization of semiconductor devices for nonlinear frequency conversion. Two kinds of parametric sources have been presented and compared: (1) a form-birefringent GaAs/AlOx waveguide for type-I parametric down-conversion, with a pump at 1 μm and signal around 2 μm; and (2) an AlGaAs waveguide for type-II parametric down-conversion, with an unguided pump at 775 nm that is noncollinearly phase-matched with a pair of counterpropagating signal and idler guided modes around 1.55 μm. Today, the former, with its high efficiency and low losses, is the more promising candidate for semiconductor guided-wave parametric amplifiers and oscillators. The latter, with its narrow bandwidth, easy collection of the down-converted photons, and tuning with a parameter as practical as the angle of incidence of the pump beam, constitutes a new archetype of integrated source of entangled photon pairs.

Acknowledgements

We acknowledge H. Zbinden, J. Van Houwelingen and J.P. Likforman for experimental help, and P. Filloux and C. Manquest for waveguide fabrication.

References

[1] S.J.B. Yoo, IEEE J. Lightwave Technol. 14 (1996) 955.
[2] W.D. Chen, J. Burie, D. Boucher, Spectrochim. Acta A 55 (1999) 2057.
[3] A. Arie, K. Fradkin-Kashi, Y. Shreberk, Opt. Laser Eng. 37 (2002) 159.
[4] D.G. Lancaster, D. Richter, F.K. Tittel, Appl. Phys. B 69 (1999) 459.
[5] N. Gisin, G. Ribordy, W. Tittel, H. Zbinden, Rev. Mod. Phys. 74 (2002) 145.
[6] A.V. Sergienko, G.S. Jaeger, Contemp. Phys. 44 (2003) 341.
[7] R.L. Sutherland, Handbook of Nonlinear Optics, Marcel Dekker, 1996.

[8] P.A. Franken, A.E. Hill, C.W. Peters, G. Weinreich, Generation of optical harmonics, Phys. Rev. Lett. 7 (1961) 118.
[9] R.C. Miller, Optical second harmonic generation in piezoelectric crystals, Appl. Phys. Lett. 5 (1964) 17.
[10] V.G. Dmitriev, G.G. Gurzadyan, D.N. Nikogosyan, Handbook of Nonlinear Optical Crystals, second ed., Springer-Verlag, Berlin, 1997.
[11] T.L. Penner, H.R. Motschmann, N.J. Armstrong, M.C. Ezenylimba, D.J. Williams, Efficient phase-matched second-harmonic generation of blue light in an organic waveguide, Nature 367 (1994) 49.
[12] G. Khanarian, R.A. Norwood, D. Haas, B. Feuer, D. Karim, Phase-matched second-harmonic generation in a polymer waveguide, Appl. Phys. Lett. 57 (1990) 977.
[13] U. Meier, M. Bösch, Ch. Bosshard, F. Pan, P. Günter, Parametric interactions in the organic salt 4-N,N-dimethylamino-4′-$N′$-methyl-stilbazolium tosylate at telecommunication wavelengths, J. Appl. Phys. 83 (1998) 3486.
[14] J.A. Armstrong, N. Bloembergen, J. Ducuing, P.S. Pershan, Interactions between lightwaves in a nonlinear dielectric, Phys. Rev. 127 (1962) 1918.
[15] L.E. Myers, M.L. Bortz, M.A. Arbore, R.C. Eckardt, M.M. Fejer, R.L. Byer, Quasi-phasematched optical parametric oscillators in periodically poled $LiNbO_3$, Optics and Photonics News (30 December 1995).
[16] C. Canalias, V. Pasikevicius, Counter-propagating QPM parametric interactions: A mirrorless OPO in sub-μm periodically-poled $KTiOPO_4$, CLEO 2007 postdeadline paper CPDB12, Baltimore, May 6–11, 2007.
[17] L.A. Eyres, P.J. Tourreau, T.J. Pinguet, C.B. Ebert, J.S. Harris, M.M. Fejer, L. Becouarn, B. Gerard, E. Lallier, All-epitaxial fabrication of thick, orientation-patterned GaAs films for nonlinear optical frequency conversion, Appl. Phys. Lett. 79 (2001) 904.
[18] M.A. Arbore, M.M. Fejer, Singly resonant optical parametric oscillation in periodically poled lithium niobate waveguides, Opt. Lett. 22 (1997) 151.
[19] B. Agate, E.U. Rafailov, W. Sibbett, S.M. Saltiel, P. Battle, T. Fry, E. Noonan, Highly efficient blue-light generation from a compact, diode-pumped femtosecond laser by use of a periodically poled KTP waveguide crystal, Opt. Lett. 28 (2003) 1963.
[20] L. Scaccabarozzi, M.M. Fejer, Y. Huo, S. Fan, X. Yu, J.S. Harris, Enhanced second-harmonic generation in AlGaAs/Al_xO_y tightly confining waveguides and resonant cavities, Opt. Lett. 31 (2006) 3628.
[21] I. Shoji, T. Kondo, A. Kitamoto, M. Shirane, R. Ito, Absolute scale of second-order nonlinear-optical coefficients, J. Opt. Soc. Am. B 14 (1997) 2268.
[22] D.S. Hum, M.M. Fejer, Quasi-phasematching, C. R. Physique 8 (2007) 180–198.
[23] J. Van der Ziel, Appl. Phys. Lett. 26 (1975) 60.
[24] J.M. Dellesasse, J.N. Holonyak, A.R. Sugg, T.A. Richard, N. El-Zein, Appl. Phys. Lett. 57 (1990) 2844.
[25] A. Fiore, V. Berger, E. Rosencher, P. Bravetti, J. Nagle, Nature 39 (1998) 463.
[26] A. De Rossi, V. Berger, G. Leo, G. Assanto, IEEE J. Quantum Electron. 41 (2005) 1293.
[27] A. Fiore, V. Berger, E. Rosencher, P. Bravetti, N. Laurent, J. Nagle, Appl. Phys. Lett. 71 (1997) 3622.
[28] A. De Rossi, V. Berger, M. Calligaro, G. Leo, V. Ortiz, X. Marcadet, Appl. Phys. Lett. 79 (2001) 3758.
[29] S. Venugopal Rao, K. Moutzouris, M. Ebrahimzadeh, A. De Rossi, G. Gintz, M. Calligaro, V. Ortiz, V. Berger, Influence of scattering and two-photon absorption on the optical loss in GaAs/Al_2O_3 nonlinear waveguides measured using femtosecond pulses, IEEE J. Quantum Electron. 39 (2003) 478.
[30] O. Durand, F. Wyckzisk, J. Olivier, M. Magis, P. Galtier, A. De Rossi, M. Calligaro, V. Ortiz, V. Berger, G. Leo, G. Assanto, Contraction of aluminum oxide thin layers in optical heterostructures, Appl. Phys. Lett. 83 (2003) 2554–2556.
[31] A. De Rossi, V. Ortiz, M. Calligaro, L. Lanco, S. Ducci, V. Berger, I. Sagnes, J. Appl. Phys. 97 (2005) 073105.
[32] P. Baldi, M. Sundheimer, K. El Hadi, M.P. de Micheli, D.B. Ostrowsky, Comparison between difference-frequency generation and parametric fluorescence in quasi-phase-matched lithium niobate waveguide, IEEE J. Select. Top. Quant. Electron. 2 (1996) 385.
[33] Y.J. Ding, S.J. Lee, J.B. Khurgin, Phys. Rev. Lett. 75 (1995) 429.
[34] S. Venugopal Rao, K. Moutzouris, M. Ebrahimzadeh, A. De Rossi, G. Gintz, M. Calligaro, V. Ortiz, V. Berger, Opt. Commun. 213 (2002) 223.
[35] A. De Rossi, V. Berger, Phys. Rev. Lett. 88 (2002) 043901.
[36] M.C. Booth, A. Atatüre, G. Di Giuseppe, B.E.A. Saleh, A.V. Sergienko, M. Teich, Phys. Rev. A 66 (2002) 023815.
[37] M. Ravaro, Y. Seurin, S. Ducci, G. Leo, V. Berger, A. De Rossi, G. Assanto, J. Appl. Phys. 98 (2005) 063103.
[38] E. Knill, R. Laflamme, G.J. Milburn, Nature 409 (2001) 46.
[39] P.G. Kwiat, K. Mattle, H. Weinfurter, A. Zeilinger, A.V. Sergienko, Y.H. Shih, Phys. Rev. Lett. 75 (1995) 4337.
[40] L. Lanco, S. Ducci, J.-P. Likforman, M. Ravaro, P. Filloux, X. Marcadet, G. Leo, V. Berger, Appl. Phys. Lett. 89 (2006) 031106.
[41] S. Adachi, in: S. Adachi (Ed.), Properties of Gallium Arsenide, INSPEC, London, 1993.